Optimizing multiple beam interferometry in the surface forces apparatus: Novel optics, reflection mode modeling, metal layer thicknesses, birefringence, and rotation of anisotropic layers Ⓕ

ⓘ Kai A. Schwenzfeier, Andreas Erbe, ⓘ Pierluigi Bilotto, ⓘ Maximilian Lengauer, Claudia Merola, ⓘ Hsiu-Wei Cheng, ⓘ Laura L. E. Mears, ⓘ Markus Valtiner, et al.

COLLECTIONS

Ⓕ This paper was selected as Featured

View Online   **Export Citation**   **CrossMark**

ARTICLES YOU MAY BE INTERESTED IN
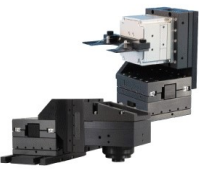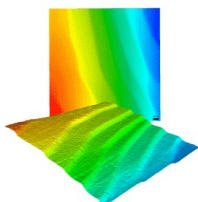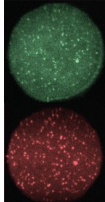
A 3-mirror surface force balance for the investigation of fluids confined to nanoscale films between two ultra-smooth polarizable electrodes
Review of Scientific Instruments **89**, 123901 (2018); https://doi.org/10.1063/1.5045485

High-density diffuse optical tomography for imaging human brain function
Review of Scientific Instruments **90**, 051101 (2019); https://doi.org/10.1063/1.5086809

High-pressure laser floating zone furnace
Review of Scientific Instruments **90**, 043906 (2019); https://doi.org/10.1063/1.5085327

MCL MAD CITY LABS INC. www.madcitylabs.com

Nanopositioning Systems   Modular Motion Control   AFM and NSOM Instruments   Single Molecule Microscopes

Optimizing multiple beam interferometry in the surface forces apparatus: Novel optics, reflection mode modeling, metal layer thicknesses, birefringence, and rotation of anisotropic layers Ⓕ

Kai A. Schwenzfeier,[1,a] ⒾⒹ Andreas Erbe,[2,b),c] ⒾⒹ Pierluigi Bilotto,[1] ⒾⒹ Maximilian Lengauer,[1] ⒾⒹ Claudia Merola,[1] Hsiu-Wei Cheng,[1] ⒾⒹ Laura L. E. Mears,[1] ⒾⒹ and Markus Valtiner[1,d] ⒾⒹ

AFFILIATIONS

[1] Institute for Applied Physics, Vienna University of Technology, Wiedner Hauptstrasse 8-10, A-1040 Vienna, Austria
[2] Department of Material Science and Technology, Norwegian University of Science and Technology, NO-7491 Trondheim, Norway

[a] Electronic mail: kai.schwenzfeier@tuwien.ac.at
[b] Electronic mail: SFA-explorer@the-passivists.org
[c] Also at: Max-Planck-Institut für Eisenforschung GmbH, Max-Planck-Str. 1, 40237 Düsseldorf, Germany.
[d] Author to whom correspondence should be addressed: markus.valtiner@tuwien.ac.at

ABSTRACT

Multiple beam interferometry (MBI) evolved as a powerful tool for the simultaneous evaluation of thin film thicknesses and refractive indices in Surface Forces Apparatus (SFA) measurements. However, analysis has relied on simplifications for providing fast or simplified analysis of recorded interference spectra. Here, we describe the implementation of new optics and a generalized fitting approach to 4×4 transfer matrix method simulations for the SFA. Layers are described by dispersive complex refractive indices, thicknesses, and Euler angles that can be fitted, providing modeling for birefringent or colored layers. Normalization of data by incident light intensities is essential for the implementation of a fitting approach. Therefore, a modular optical system is described that can be retrofit to any existing SFA setup. Real-time normalization of spectra by white light is realized, alignment procedures are considerably simplified, and direct switching between transmission and reflection modes is possible. A numerical approach is introduced for constructing transfer matrices for birefringent materials. Full fitting of data to the simulation is implemented for arbitrary multilayered stacks used in SFA. This enables self-consistent fitting of mirror thicknesses, birefringence, and relative rotation of anisotropic layers (e.g., mica), evaluation of reflection and transmission mode spectra, and simultaneous fitting of thicknesses and refractive indices of media confined between two surfaces. In addition, a fast full spectral fitting method is implemented for providing a possible real-time analysis with up to 30 fps. We measure and analyze refractive indices of confined cyclohexane, the thickness of lipid bilayers, the thickness of metal layers, the relative rotation of birefringent materials, contact widths, as well as simultaneous fitting of both reflection and transmission mode spectra of typical interferometers. Our analyses suggest a number of best practices for conducting SFA and open MBI in an SFA for increasingly complex systems, including metamaterials, multilayered anisotropic layers, and chiral layers.

I. INTRODUCTION

Thin film studies using multiple-beam interferometry (MBI) evolved as a powerful tool for measuring absolute thicknesses and complex refractive indices, $\tilde{n}$, of nanometer confined thin films between apposing surfaces.

Since the first analysis of MBI patterns by Tolansky,[1] the technique has further evolved to study surface and interfacial forces in

biological and engineering environments. Implemented in the Surface Forces Apparatus (SFA), which was pioneered by Tabor, Winterton, and Israelachvili,[2–4] MBI provided direct quantification of fundamental interaction forces across surfaces and thin-film properties down to separation distances D below 1 nm, including the first measurement of van der Waals forces,[5] hydration layering,[6] or hydrophobic interactions.[7] Other applications included polymers in solution,[8] the experimental verification of the Kelvin equation,[9] and Derjaguin-Landau-Verwey-Overbeek (DLVO) forces.[10]

As shown in Figs. 1(a) or 1(b), in a typical SFA experiment, two 90°-crossed silica cylinders, covered with back-silvered transparent mica surfaces, are brought into contact. The central aspect of the SFA experiment is that the apposing surfaces are set up in such a way that they form an interferometer for MBI. White light is then transmitted perpendicular to the apposing surfaces, resulting in standing waves forming fringes of equal chromatic order (FECO) that can be recorded with an ordinary imaging spectrometer. Variation of absolute separation distances D of apposing surfaces can subsequently be measured by tracking wavelength shifts of FECO.[4]

Figure 1(c) shows an overview of possible options for combining optical slabs for establishing interferometers for transmission and reflection mode operation in SFA (cf. the figure for details).

In the transmission mode, fluids with thickness, Λ_{gap}, and complex refractive index, $\tilde{n}_{gap}$, are frequently confined between transparent layers of uniformly thick muscovite mica ($\Lambda_2 = \Lambda'_2$ with a complex refractive index of $\tilde{n}_2 = \tilde{n}'_2$). Semi-transparent silver mirrors, henceforth, referred to as "mirrors," with thicknesses $\Lambda_1 = \Lambda'_1$ = 30–55 nm, are applied to the backside of the mica layers. Using MBI then allows the measurement of the thickness of the mica layers (at $\Lambda_{gap} = 0$) and subsequently the distance between surfaces defined as $D = \Lambda_{gap}$.

Simultaneously, normal forces, $F(D)$, as well as contact radii, R, between the surfaces can be measured using MBI.[4,11] Strain gauges are often implemented for detecting friction forces.[11] A typical flow chart of various SFA experiments and a flow of the accompanying analysis are shown in Fig. S1 of the supplementary material.

Muscovite mica has been used as a transparent material because it is relatively simple to prepare uniformly thick and atomically smooth layers.[2] Mica layers are typically cleaved to thicknesses ranging from 3 to 6 μm. Mica can be further chemically modified introducing additional thin layers on both or one of the apposing surfaces, establishing either symmetric or asymmetric interferometers, respectively. The resulting thin-film modifications have defined thicknesses (Λ_m and/or Λ'_m) and refractive indices ($\tilde{n}_m$ and $\tilde{n}'_m$) and can be applied using a number of approaches including formation of supported lipid bilayers[12] as well as self-assembled silane monolayers.[13,14]

Another frequently used interferometer layout is formed by facing one back-silvered mica surface against a smooth metal surface (usually, e.g., gold, platinum, and palladium) templated from mica[15,16] or evaporated by magnetron sputtering or physical vapor deposition (PVD). The latter also has a surface roughness of σ_{rms} = 1–2 nm, while templated surfaces are smooth with σ_{rms} < 0.5 nm.[15] In such a setup, it is again possible to introduce chemical surface modifications, such as self-assembled monolayers on gold[14] or modifications used for mica, resulting again in asymmetric/symmetric interferometers.

A reflection mode interferometer can be formed, e.g., by using a bulk metal that faces a back-silvered mica surface. This setup has so far been tested in only one set of experiments by Horn et al.[17] where shape-changes of mercury-drops were induced electrochemically. With the increasing interest in electrochemical interfaces and
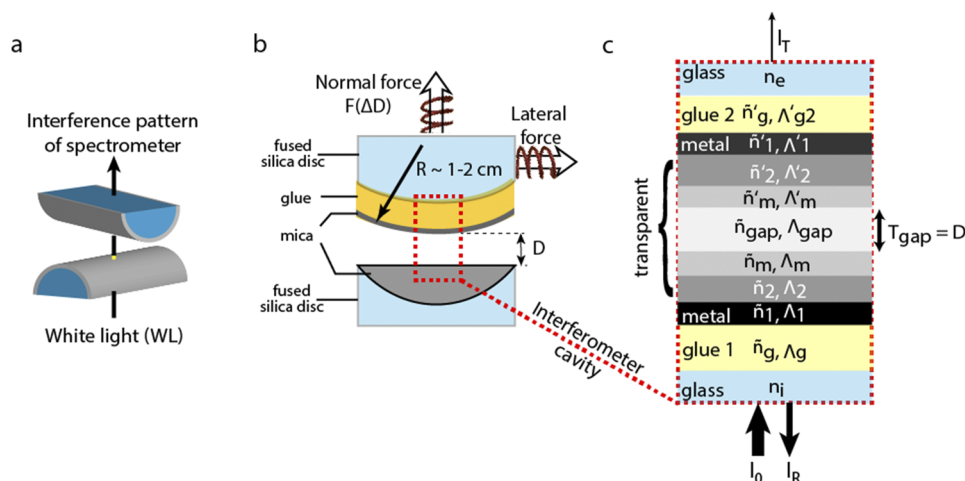

FIG. 1. (a) The typical sample geometry in SFA experiments is a crossed cylinder geometry. (b) Absolute distance, D, the contact radius, R, and lateral as well as normal force are measured in an SFA experiment. (c) Typical options for interferometer stacks in transmission and reflection modes consist of up to 2–7 layers in the transmission mode and 2–5 layers in the reflection mode, depending on whether specific surface modifications are applied or not. Reflective metal mirrors (Λ_1/Λ'_1) are essential for establishing an interferometer cavity. They are semitransparent with $\Lambda_1 = \Lambda'_1 \approx$ 30–55 nm. While in the reflection mode, one bulk metal layer with $\Lambda'_1 \rightarrow \infty$ is used. Any number of transparent layers, that can be stacked between the metals, necessarily have a combined thickness $\geq$2–3 times the wavelength of the light used, in order to establish resonance in the wavelength range used. In a typical SFA experiment, forces F are measured as a function of a fluid gap layer thickness Λ_{gap} that defines the absolute surface separation $D = \Lambda_{gap}$. The layers between the metal mirrors can be set up in many different ways, and the glue layer indicated in (b) is usually chosen in such a way that it has a refractive index close to glass (cf. the text for details in Sec. III B).

corrosion studies,[18,19] oxide covered bulk metal samples became increasingly important in SFA experiments. However, no rigorous treatment exists for such interferometers.

Hence, a rich variety of sample and interferometer preparations is by now available for SFA experiments. The various interferometers consist of layered stacks of materials with different optical properties, and calculating thin film thicknesses needs to take into account all of the layers and their wavelength dependent change of optical properties.

For SFA experiments, analysis typically utilized simplified equations for interferometers with 2–7 layers, with wavelength independent optical properties.[4] A number of researchers independently developed more rigorous analysis approaches[20,21] based on an algorithm using a 2×2 multiple matrix method by Born and Wolf.[22] Heuberger extended the use of 2×2 matrix based analysis and developed the fast correlation spectroscopy (FCS) method to provide fast and online analysis of interference patterns recorded in SFA.[23,24] In this technique, the maximum intensity patterns are read out and fitted to simulated spectra, and also secondary and tertiary interference patterns can be fitted. The 2×2 multiple matrix method is, however, not suited for fitting, e.g., birefringent materials, such as mica or anisotropic fluid layers, which is often essential for SFA measurements and could open a number of new possibilities.

Recently, Zappone et al.[25] rederived matrices designed for more complex fluids with continuously twisting optical parameters and discussed a qualitative resemblance with measured spectra analyzed by peak tracking. However, a somewhat different approach to evaluate transmission coefficients compared to Schubert[26] was applied in this work. In addition, Kuhl et al. developed methods for describing layers with varying refractive indices.[27,28]

Already in 1996, Schubert[26] derived a 4×4 transfer matrix that provides a unified theoretical approach to electromagnetic plane waves reflected or transmitted at arbitrarily anisotropic and homogeneous layered systems. This work explicitly already includes partial transfer matrices for a slab of a continuously twisted biaxial material at normal incidence, and arbitrary isotropic and randomly distributed anisotropic slabs, as well as incident and exit matrices. We previously applied this approach to model only a few monolayer-thin, oxide layers formed electrochemically on various noble metals.[16]

Here, we discuss the implementation of novel optics for the SFA and implement the Schubert matrix method for fitting MBI data from SFA experiments. We show that it is possible and essential to rigorously treat mica in SFA experiments, which is a natural material, with naturally varying optical parameters. Specifically, in experiments, mica naturally displays a considerable variation of refractive indices and birefringence even from experiment to experiment. Here, we demonstrate (i) a self-consistent fitting of birefringence and anisotropic mica refractive indices and (ii) a full fitting of the observed spectra to minimize errors from data treatment (including fitting of mirror thicknesses and refractive indices of confined fluids). On selected examples, we discuss how a full fitting procedure, as compared to a peak correlation analysis, affects the interpretation of SFA results.

The analysis code described in this study is developed to work with freely available optical databases that provide wavelength dependent optical parameters. Implementation of Schubert's approach, which is well established and tested in other fields, will open MBI for increasingly complex systems, e.g., with transfer matrices readily at hand for metamaterials, arbitrarily multilayered and anisotropic layers or chiral layers.

II. METHODS, MATERIALS, AND HARDWARE

A. Chemicals and materials

Highest available purity chemicals (NaCl, cyclohexane, ethanol, hexane, and hexadecane-1-thiol) were used as received from Sigma Aldrich, unless otherwise specified. Milli-Q water (Millipore, a resistivity of ≥ 18 MΩ cm^{-1}, TOC below 2 ppb) was used for preparing NaCl solutions (pH = 5.5–5.7 and concentration 10 mM). 1,2-dipalmitoyl-sn-glycero-3-phosphocholine (DPPC) was obtained from Avanti Lipids and was stored at -20 °C. Mica was obtained from SJ Trading Company (NJ, USA) as approximately 20×10 cm reddish colored sheets with 2–3 mm thickness.

B. Surface Forces Apparatus

SFA normal force measurements were performed at 24 °C using the SFA 2000 (SurForce LLC, Santa Barbara, CA). The relative angular rotation can be varied with an accuracy and repetition of $\pm 2°$. The optical setup consists of several beam splitters, optical rail systems, irises, $4\times$ and $10\times$ microscope objectives (Nikon), a light-emitting diode (LED) cold white light source, a low-pass filter to filter any wavelength above 650 nm, and an Andor EM-CCD sensor (338 iXon) and spectrometer (300 mm or 500 mm focal distance, 300 lines/mm up to 1800 lines/mm gratings with blaze angles around 550 nm). The effective resolution of our spectrometer/camera combinations is in the range of 0.04–0.02 nm, depending on the grating used.

Mica sheets were hand-cleaved to provide sheets with an area of several (typically 5–10) cm^2 and uniform thicknesses ranging from 4 to 6 μm. The edges of these sheets were melt-cut with a hot platinum wire. Particular care was taken to avoid contamination of the mica sheets with platinum particles. With the use of PVD (see below for this model), the mica sheets were back-silvered with a 40 ± 2 nm silver layer and then glued to cylindrical silica disks with a nominal radius of curvature $R = 1$–2 cm, using an UV curable glue (Norland Adhesives, NOA81, $n_g = 1.56$).

C. Self-assembled monolayer and Langmuir-Blodgett deposition

Atomically, smooth gold films were prepared by template stripping as previously described.[14] Freshly stripped gold surfaces were placed immediately into a 1 mM solution of hexadecane-1-thiol, resulting in a hydrophobic surface termination. Exposure of the solution to light was avoided during the reaction time. After 12–24 h, the surfaces were taken out of the solution, washed with hexane and ethanol, and mounted into the SFA.

Langmuir-Blodgett layers of DPPC were transferred in their gel-phase at 40 mN/m using a R&K LB-trough (Riegler and Kirstein, Potsdam, Germany).

D. Other techniques and instrumentation

An Abbe5 refractometer (VWR International) was used to measure the refractive index of fluids with 0.5×10^{-4} accuracy.

An in-house designed PVD, manufactured by BestTec (Berlin, Germany), was used for depositing metal layers. The base pressure of the chamber is 1×10^{-8} mbar, and during deposition, samples are rotated at 30 rpm, with a distance of 50 cm from a 10 kW electron beam source. This results in a film uniformity of $\Delta\Lambda_1 \leq 5\%$ over 1 cm.

E. Simulation and fitting approach

For the transfer matrix approach, which is described in Figs. S2 and S3 and reviewed in detail in the related text of the supplementary material, we implemented a home-made graphical user interface ("SFA Explorer").

Simulated spectra are fit against measured spectra by minimizing the root mean squared deviation using a Levenberg-Marquardt algorithm implemented in the Python lmfit-library.[29] Since the measured spectra are usually in counts, instead of transmittance as simulated, we scale the intensity to a pseudotransmittance using a linear model and thus add a scaling and an offset parameter. In addition, and as will be shown below, it is essential to include a normalization of the measured data by a reference white light spectrum.

F. Python packages and hardware

The analyses were made using home-written software (SFA Explorer) that was used within a WinPython-3.4.4.6[30] python distribution with added PySide-1.2.4[31] (via pypi.org). The modules; numpy-1.11.3+mkl,[32] scipy-0.18.1,[33] pillow-4.0.0,[34] pyqtgraph-0.10.0,[35] and lmfit-0.9.5,[29] were already supplied by the WinPython distribution. Analysis and benchmarks were performed on a standard office personal computer (PC) with Microsoft Windows 10[TM], an Intel i7[TM] processor, and 16 GB RAM, with a 7000 rpm HDD.

G. Optical data for simulations

The optical data used for the simulations of silver,[36] gold,[36] cyclohexane,[37] water,[38] DPPC,[39] fused silica,[40] and air[41] were taken from refractiveindex.info,[42] converted to wavenumbers, and reformatted. A wavelength independent refractive index for the Norland Products optical glue NOA81 has been taken from Ref. 43. Refractive indices for mica were fitted using the empirical equation from Ref. 44 as a reference for the wavelength dependence and varying the absolute value and the splitting between the crystallographic distinct refractive indices β and γ, which are perpendicular to the crystallographic c-direction. For the silver layers, the optical data from Rakić et al.[36] were chosen. We find that this optical data set is capable of fitting all observed features of the experimental spectra, while others are not. Details are discussed in Sec. III.

III. AN OPTICAL SYSTEM FOR TRANSMISSION AND REFLECTION MODE SURFACE FORCES APPARATUS EXPERIMENTS

While much work has been invested in improving the design of various SFAs over the past few decades, relatively little to nothing has been done to further advance the optical performance of SFA experiments. As discussed above, previous data analysis in the SFA focused on peak correlation and/or simplified equations. No quantitative attempt has been made to fully fit the observed

spectra to 4×4 transfer matrix simulations, taking into account, e.g., anisotropy mica and confined thin films. For providing the capacity to fit full SFA spectra, rather than spectral maxima,[4,11,23] it is essential to normalize the recorded spectra. Specifically, simulations based on the transfer matrix method compute normalized transmittance ($T = I_T/I_0$) and reflectance ($R = I_R/I_0$), while SFA data are usually not normalized, showing strong intensity variations over the spectrum. An inspection of the spectral properties of typical white light sources used in SFA, shown in Fig. S4 of the supplementary material, reveals strong wavelength dependent intensity variations and suggests that a full simulation of SFA data requires a normalization by a reference white light spectrum that is transmitted through the SFA optics used. Hence, traditional optics of an SFA have to be upgraded as follows.

A. Improving of optics for SFA measurements and MBI analysis

Figure 2 describes the implementation of both standard transmission mode operation and reflection mode operation, which means to provide *in operando* normalization of data by white light reference spectra and simplification of alignment of optics. Specifically, Fig. 2 compares the optical path designed for SFA experiments in the (a) transmission and (b) reflection modes. This setup introduces two essential and novel aspects.

First, in classic SFA experiments,[2–4] the optical system is composed of a white light source, heat filter, the SFA chamber, a free standing microscope, and one or two prisms to guide the light path emerging from the microscope to a spectrometer. Perpendicular beam alignment is in fact very tedious and error-prone in such a setup. Small deviations from a perpendicular light path can, however, result in often significant distance shifts. Specifically, if a contact position is changed within an experiment, which is a frequent procedure, realignment of the path results in artificial shifts of the recorded peak wavelength, and hence, shifts in distance in the 0.5–1 nm range. Furthermore, finding a contact position and realignment of the optics require significant training. Our upgraded optical system, Fig. 2, fixes all optical paths using a standard cage system, which can be aligned perfectly perpendicular using a set of irises and beam guides. As a result, we always move established contacts (i.e., interferometric cavities) into the center of the optimized optical path, as indicated by the red line in Fig. 2. For this, the SFA itself is mounted on a x/y translation stage. This simplifies the optical alignment of the SFA considerably. As soon as any established contact position is moved into the center position, both FECO and Newton's rings recorded with the spectrometer and camera, respectively, are immediately observed. This simplifies searching for contact positions and even provides a pathway for automating the approach and alignment procedures. The optical system also provides a flexible platform for easily adding new capabilities such as fluorescence microscopy[45] or laser interferomerty.[46–48]

A second important addition to existing SFA optics is the simultaneous, yet fully decoupled, measurement of reference lines and the white light source spectra. For this, beam paths are included, guiding 10% of the white light and a reference light, directly into the spectrometer. Both beams are laterally translated and shaped using translating pinholes and slits. Lateral translation of the reference and white light beam allows us to project these beams at the upper and lower halves of the sensor, while the MBI signal is projected into
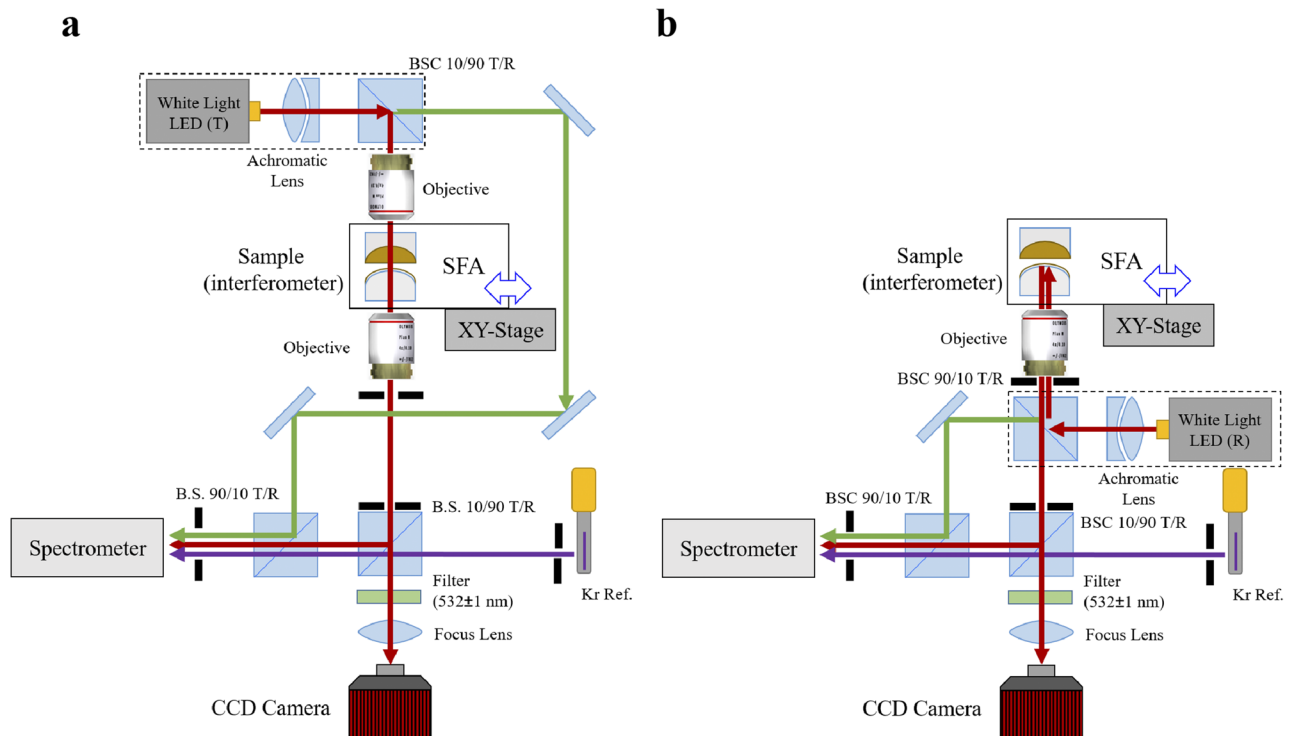
FIG. 2. Newly designed modular optics for recording (a) transmission mode and (b) reflection mode spectra, simplified "all-perpendicular" beam alignment and simultaneous FECO and microscopy recording. Red lines indicate the white light path through the interferometer into the camera/spectrometer. The green line reflects the white light reference path, and the reference (typically krypton or mercury) is colored in purple. Important optical elements such as beam splitter cubes (BSC) as well as irises for beam alignment are indicated (cf. the text for details and a photograph is given in Fig. S5 of the supplementary material).

the center of the sensor. As a result, and as shown in Fig. 3, we can simultaneously record reference lines, white light spectra, and FECO. This procedure eliminates any fluctuations of the source during data normalization. Specifically, if the source fluctuates, both FECO and white light spectra similarly fluctuate, maintaining the transmittance constant.

All data shown below are normalized by an appropriate reference white light beam, to allow for a full fitting of the entire spectra.

B. Inspection of the influence of glue and glass layers supporting the interferometer

So far, all simulation and analysis approaches in SFA ignored the effect of glue layers and fused silica discs, which encase the interferometer cavity. Only recently, glue layer effects were inspected in terms of relative peak ratios for a special 3-mirror interferometer.[49] An important question for judging the absolute accuracy of an SFA measurement is, however, how much varying support layer thicknesses may shift the measured resonances. Experimentally, specifically the glue thickness is virtually impossible to control within a submicrometer uniformity. Glue layers may not have similar thicknesses for both supporting layers, and they may change significantly during change of contact positions, which is a standard procedure in SFA, specifically if additional layers are introduced. In such a case, it is essential to unmount/remount a sample, and with high certainty, a

slightly different contact point will be established. Resulting artificial shifts will lead to in a significant absolute error. Here, we quantify the extent of this systematic error.

Figure 4 investigates the effect of the glass and a varying glue layer [see again Fig. 1(c)], to evaluate principle effects on the patterns in the data. The support layers impose a difference in the refractive index transitions between the interferometer and its environment.

For comparison, a typical 3-layer (mica | mica) interferometer has been modeled with and without the supporting layers. Figure 4(a) shows the simulated spectra without any supporting layers (no glue), as used elsewhere, and for different symmetric glue thicknesses with a refractive index of 1.56 typical for UV-curing hard epoxy glues after curing.

Figure 4(a) compares the interferometer with and without supporting layers and how resulting spectral positions of the FECO shift and how the $\beta-\gamma$ splitting varies.

First, due to the introduction of a glue layer, all peaks show a relative shift to lower wavelengths, which is due to the change of the phase shift compared to modeling with a semi-infinite layer of air.

Second, the $\beta-\gamma$ splitting introduced by the birefringence of the mica appears to increase in the presence of the supporting layers as well. This can also be attributed to the differences in refractive indices at the additional interfaces, resulting in different phase shifts.

Third, additional weak interference patterns of two different orders are superimposed compared to the spectrum with no glue and
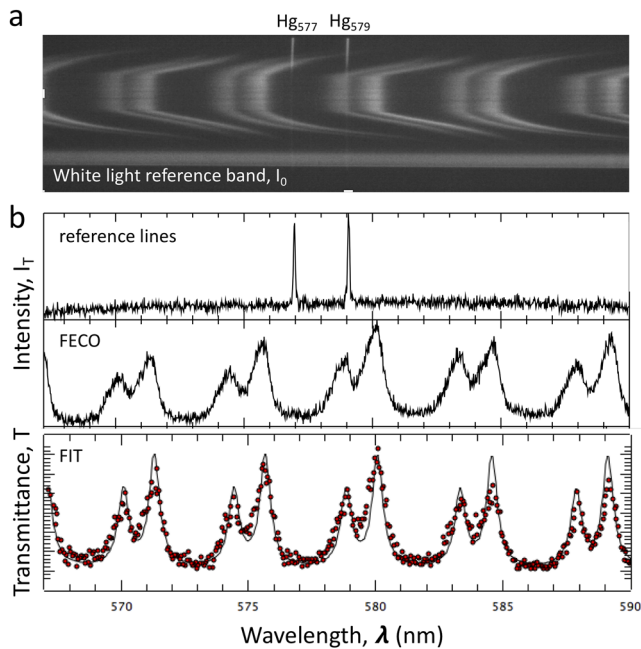
FIG. 3. (a) FECO recorded for a mica | mica contact in water. The spectrum also shows the simultaneously recorded white light reference band and the reference lines. Paths for these beams are translated and shaped so that they do not interfere with the FECO recorded in the center of the sensor. (b) Intensity profile of FECO in contact, as well as calculated transmittance $T = I_T/I_0$, along with a fit (solid line) using the 4×4 transfer matrix approach.
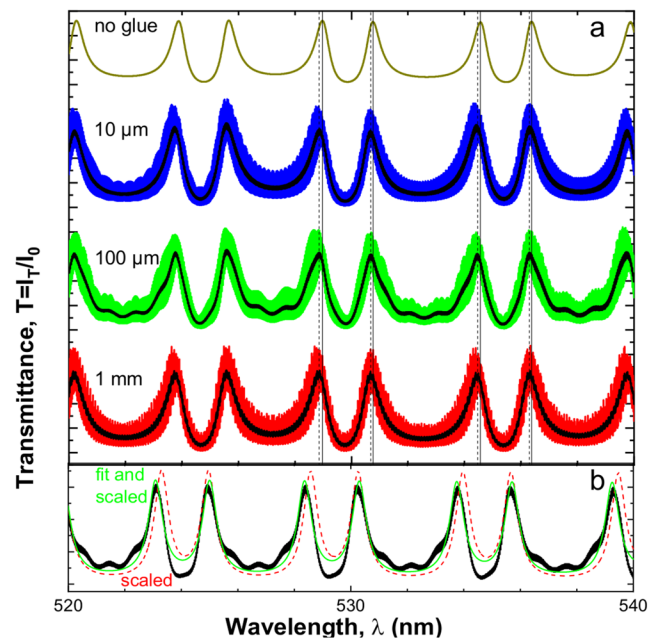

FIG. 4. Simulated spectra for an interferometer formed from layers as shown in Fig. 1. In (a), a spectrum has been simulated without any supporting layers (no glue) and others with a 3 mm glass layer and varying thicknesses of the glue layer (NOA81[43]), topped with mica and with a water layer as the gap medium of 20 nm. Colored lines are data simulated with a resolution of 200 points/nm, and the black line is a 10 point moving average to replicate the spectrometer resolution. Vertical lines have been added at the FECO maxima of the no glue case (solid lines) and the 100 μm (dashed lines) to illustrate the small shift in position of the FECO and the change in splitting between β- and γ-fringes. The largest shift occurs upon introduction of a glue layer, minor variations as a function of the glue layer thickness are within the typical SFA noise level (cf. the text). (b) is the same interferometer with a 100 μm glue layer without a gap layer ($\Lambda_{gap} = 0$). Displayed data (black) are with the same resolution after smoothing the high order oscillations in (a). The data have been fit with the model without supporting layers, first with the same interferometer layer parameters as used for the simulations (scaled, red dashed line) and second with allowing the mica thickness and birefringent splitting parameters to fit freely (fit and scaled, green line).

glass layer: a high order interference arises from internal reflections within the glass support and a lower order modulation arises from the reflections between the mirror and glass across the glue layer. As can be seen in all spectra simulated with glue, the high order signal superimposes a pattern oscillating with a 0.001 nm periodicity (not visible with the plotted magnification), which is independent of the glue thickness. This signal arises from the 3 mm thickness of the glass disks. The generated pattern is however not detectable in the recorded spectra due to the resolution limitations of the spectrometers, which are in the range of 0.02–0.04 nm (depending on exact settings). To replicate this limitation, we used a moving average of the simulated high resolution data (solid lines in Fig. 4). As shown, the data indicate that the 3 mm thick glass surfaces have a very limited influence on spectra, below the typical noise level of SFA.

Asymmetric glue thicknesses superimpose an additional pattern onto the variability of the intensity of the supporting layer interference patterns. There is a shift in the patterns across the spectrum with increasing difference between the two glue layer thicknesses (cf. Fig. S6 of the supplementary material).

Hence, we can conclude that simplifying the interferometer to a free floating unit in air, i.e., without supporting layers, introduces an inaccuracy in the fitted parameters. In Fig. 4(b), we quantify this inaccuracy and consider the fitting of the simulated data from an interferometer including the supporting layers using the free floating interferometer model as a fitting model. Keeping the fitting

parameters of the free floating interferometer identical to the layers set in the simulated data (scaled, red dashed line), the fit quality is clearly decreased.

If mica thickness and birefringent splitting parameters are allowed to fit freely (fit and scaled, green line), a good fit can be achieved. The resulting mica thickness is fitted to be 7998.64 nm instead of the expected 8000 nm which corresponds to an error of 0.02%. At the same time, the birefringent splitting increases from 0.0052 to 0.0060 which corresponds to an error of approximately 15%.

The difference in mica thickness is therefore rather small and negligible, and the influence on the birefringence can be compensated for by adjusting the effective birefringence. The effective birefringence will be smaller by a factor of approximately 15%, if glue layers are not included in the simulation explicitly.

The simplification of using a free floating interferometer provides the benefit of a reduced computational cost, compared to

including the supporting layers, for minimal systematic error introduction. Also, in experiments, the glue thickness is not controllable after all. As such, choosing a glue that has a refractive index closer to, or matching, the fused silica disc n will be ideal; however, such glues are unfortunately often too soft for SFA purposes.

The central quantity for estimating a resulting systematic error of such a simplification is the absolute shift of peaks for a case with asymmetric glue layers. Asymmetric glue layers are the most likely experimental situation. A shift of a peak position due to contact position changes may be interpreted as a thickness change of a confined layer, although it may simply be the result of a move of the contact position and hence change of the "local" glue layer thickness. We evaluated peak positions at three different wavelengths in the green, yellow, and red wavelength ranges of the spectrum. The data suggest that the variation of the absolute peak positions of an explicit glue model is in the range of ±0.01 nm in the green and up to ±0.04 nm in the red wavelength range above 600 nm upon change of the glue thickness. Hence, in the green region, the error is clearly below the detection range of a typical spectrometer with a 0.02–0.04 nm resolution (depending on camera pixel size, grating, and spectrometer focus length), while it may become detectable at higher wavelengths. According to simplified equations for even and odd fringes,[4] a wavelength shift of 40 pm translates into a maximum detectable relative distance shift of 2–3 Å. In our analysis, we henceforth simplify the system using only "free floating interferometers," and note a potential systematic absolute (i.e., peak-to-peak) distance error of up to ±1–1.5 Å.

IV. *IN OPERANDO* DETERMINATION OF THE OPTICAL PROPERTIES OF MICA, RELATIVE ROTATION OF TWO APPOSING BIREFRINGENT MICA LATTICES, AND MIRROR THICKNESS

We now demonstrate the benefit of the full fitting of white-light normalized experimental SFA spectra, and we test the performance of the suggested optical system with new experiments and experiments known from the literature. Prior to discussing specific experiments, it is interesting to first analyze the properties of the birefringent muscovite mica, which is the most frequently used transparent material for SFA experiments.

A. *In Operando* determination of the mica refractive index

The absolute refractive index of the specific mica sheet used in experiments is a concern, regarding absolute measurements of distances and layer thicknesses in SFA experiments. Muscovite mica is a birefringent natural material, which has a reported birefringence of $\delta = 0.0035$–0.0052 with refractive indices in the range of $n_\beta = 1.52$–1.62 and $n_\gamma = n_\beta + \delta$ at 570 nm.[44] It is common practice to use fixed values for the mica refractive index in the range of $n = 1.56$–1.60 with a fixed β and γ splitting as measured in the experiment.[3,4,11,23,25] Using tabulated fixed values will result in errors in the determination of the absolute thickness of mica. This error will translate into errors in the determination of distances, specifically if an additional gap layer such as water is present. An independent measurement of the refractive index for the actual mica sheet used in an experiment seems useful and is possible by a simple iterative fitting approach, as shown in the flow chart in Figs. S1(d) and S1(e) of the supplementary material.

In particular, Fig. S1(e) of the supplementary material shows how the refractive index of mica can be fitted iteratively for a symmetric three layer experiment using a set of spectra with isotropic finite gap layer thicknesses.

Figures 5(a) and 5(b) show a mica spectrum and the corresponding fitting of the spectrum using two refractive indices within the reported window at 570 nm. Clearly, and as shown in Figs. 5(a) and 5(b), both refractive indices fit the data equally well if no gap layer is present. In contrast, and as shown in Figs. 5(c) and 5(d), as soon as a water gap of about 45 nm is introduced experimentally, only one refractive index fits the data well, even if the difference is
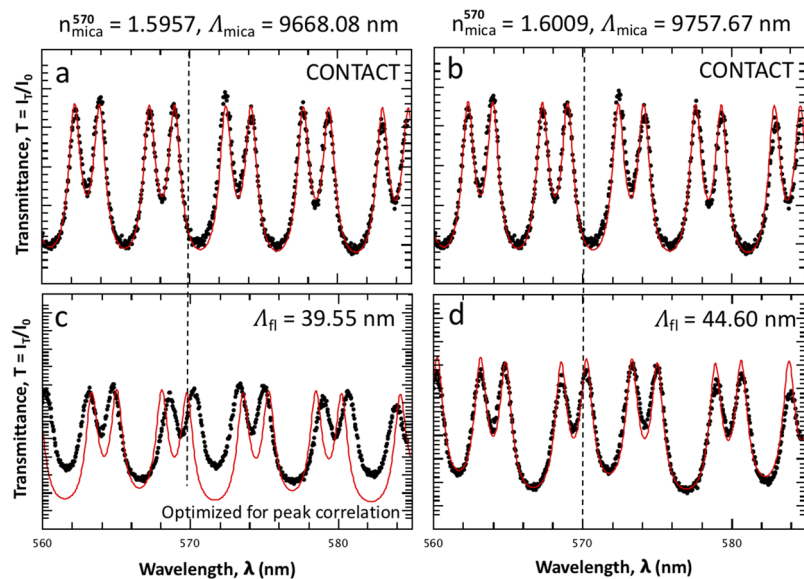
FIG. 5. Typical experimental data and fitted spectra for the same experimental data (a) or (b) at contact of two similarly thick mica sheets and (c) or (d) with a fluid (water) gap separating the two mica sheets. The fit is shown as a solid red line, and the data are plotted as points. The mica refractive indices of the γ-fringe at an example wavelength of 570 nm (cf. Sec. II G for details), the mica thickness (Λ_{mica}), and fluid gap thickness (Λ_{fl}) are fitted quantities. The dotted line is a guide line for the eye (cf. the text for details).

only $\Delta n = 5 \times 10^{-3}$. As such, an iterative fitting of mica refractive indices at $D = 0$ and at one or more larger distances, with a material in the gap with a precisely known isotropic refractive index, provides a direct *in operando* possibility to accurately measure the mica refractive index of the sheet used in a particular experiment with an accuracy of $\Delta n = 0.0002$.

Interestingly, the fitted mica thickness is off by less than 1%, while the fluid layer thickness in a three layer interferometer displays a considerably larger error of up to 10%. In addition, a close inspection of the fits indicates that specifically the even order maxima are highly sensitive to the mica refractive index, due to the finite and larger amplitude during propagation across the mica | water | mica interface. At the same time, this also suggests that a simple tracking or correlation of maxima is prone to 10% error for layer thicknesses above approximately 20–30 nm since only maxima are tracked or fitted, irrespective of the analysis method used. The mica refractive index must be fitted, in order to achieve the possible subnanometer absolute accuracy resolution of SFA also at larger distances.

B. Rotation of the mica lattice for symmetric 3–5 layer interferometers

We further test the birefringence of mica in terms of evaluating relative rotations of two equally thick apposing mica slabs. We implemented the code in such a way that the rotation of two birefringent materials can be fitted to the expected spectrum. At each iteration of the fitting routine, a new rotated transfer matrix is computed for one of the two layers using the numerical approach described above.

For qualitatively testing the performance, we purposely rotated two apposing mica layers by about $10° \pm 2°$ around the azimuthal axis. Afterward we recorded a contact in solution. Figure 3 indicates observed characteristics of the FECO pattern and transmittance. First, the rotation of the lattices is directly reflected into the intensity of the β- and γ-fringes. Here, the β-fringes show a significantly decreased intensity, and a slight shift of the wavelength of both β- and γ-fringes toward their average wavelength. Using the implemented 4×4 transfer matrix method, we can fit the rotation of the apposing mica lattices and find an effective rotation of $12°$. This matches the value targeted by the alignment of the apposing sheets. Hence, evaluating the mica birefringence in terms of intensity and peak position allows us to directly extract the relative rotation of mica lattices facing each other. This is an aspect that cannot be fitted using a peak-correlation algorithm simply because the information is obtained from the relative intensities. Commonly used peak correlation algorithms will interpret this result as a small change of the mica birefringence, which is equivalent to the wavelength shift of β- and γ-fringes. Hence, relative rotations of mica layers cannot be ignored in an analysis without the introduction of significant absolute and relative errors.

C. Influence of mirror thickness on evaluation of layer thickness

Changing metal mirror thicknesses frequently occurs in electrochemical and corrosion studies with the SFA,[16,18] and a detailed analysis of a MBI pattern can provide a very detailed understanding of chemical changes at electrified interfaces. This includes the evaluation of refractive indices of *in situ* forming metal oxides, as

well as the determination of corrosion rates by direct analysis of the degrading metal mirror thickness.

However, in analytic equations,[4,11] the thickness of the metal mirror is not taken into account and metal mirrors are treated as fully reflective with zero amplitude of propagating waves at the metal surface. This neglects phase shifts at metal interfaces, which result in shifts of standing waves if the metal mirror thicknesses change. In existing transfer-matrix based simulation approaches for MBI spectra, only the peak positions are analyzed[23] or qualitatively compared;[25] peak widths and intensities are irrelevant to the analysis.

In contrast, a full fitting approach allows us to directly analyze mirror thicknesses and resulting effects in MBI spectra. Figure 6 shows the simulated spectra of a mica | mica contact ($4 \mu m$) for an increasing thickness of (a) silver and (b) gold mirrors. First, comparing silver and gold spectra, these data show that gold mirrors result in a significantly broader FECO pattern. This is due to the significantly higher imaginary part of the refractive index (i.e., light absorption) of gold in the visible range (cf. Fig. S3 of the supplementary material). Second, upon decrease of the mirror thickness, both silver and gold show the expected increase in transmittance in combination with a significant wavelength shift of up to 1 nm for very thin mirrors. In a previous study, we have already shown how transmittance can be used to estimate the corrosion rate of a mirror used in an MBI experiment.[18]

More interestingly, in the context of this work, Fig. 6(c) also shows the mirror thickness plotted vs the wavelength shift. The characteristic shape of this plot suggests a larger influence of mirror thickness changes for thinner mirrors. We also estimate that a 5% variation in the thickness range typically used in a SFA experiment can result in up to 80 pm wavelength shift. This is an interesting result as 5% over 1 cm of the sample is a typical homogeneity obtained by an ideal PVD process (rotating sample, ideal impact angles, etc.). This suggests that changing the contact position, which is a typical practical procedure in SFA, can result in considerable absolute distance errors, using the analytic equations or peak correlation approaches. According to analytical equations[4] for even and odd fringes, a wavelength shift maximum of 80 pm (estimated as 3σ of a Gaussian distribution) results in an average shift of ± 7 Å/± 5 Å for odd/even fringes, respectively.

This does not seem significant and may be safely ignored for measurements where molecular dimensions (sub 1–2 nm distances or layer thicknesses) are not approached or studied. However, for hydration force measurements, self-assembled monolayer thicknesses, or for measuring oscillatory behavior of molecular fluids, it is, therefore, essential to carefully analyze, and if necessary, fit the mirror thickness. Otherwise, the data have to be reported with an average absolute error in the range of molecular dimensions.

In our experiments, we find a number of interesting aspects. First, silver mirrors are typically about 20% thinner compared to deposited thicknesses of 35 nm measured using a quartz balance in a well calibrated PVD. This is very likely due to the significant oxidation of the silver after exposure to ambient environment and during heat or UV curing of glues used to attach mica sheets to the cylindrical glass discs. Typical oxide thicknesses on silver are in the range of 2–10 nm depending on the exposure conditions to oxidizing environments.[50,51] An independent measurement of the silver thickness after curing is not within the scope of this work.
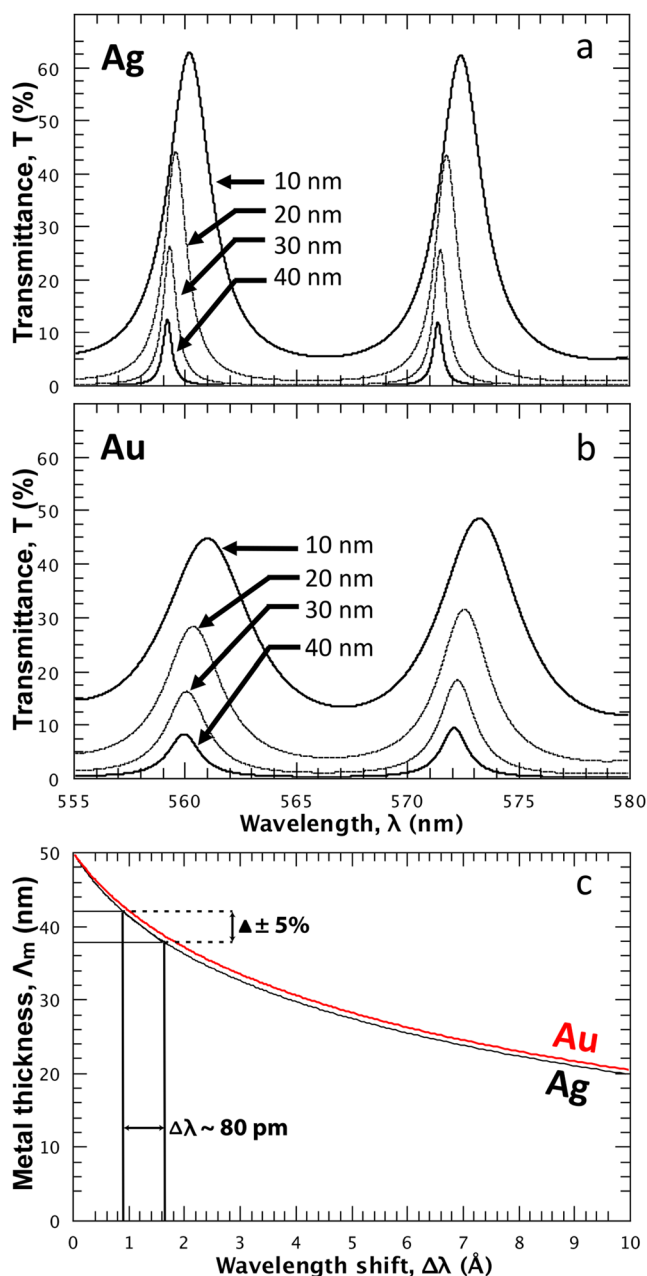
FIG. 6. Effect of metal mirror thickness on the peak shape and position for (a) silver and (b) gold interferometers. The extracted wavelength shifts are shown in (c). The spectra are calculated for a symmetric stack of two contacting mica surfaces with a thickness of 4 μm.

Second, upon changing a contact position, we usually find only about 2% mirror thickness variation, suggesting that PVD processes may be slightly better than quoted by PVD manufacturers (see Sec. II), or degradation during gluing may, to some extent, level out initial roughness.

V. EXPERIMENTAL VERIFICATION OF NEW OPTICS AND ANALYSIS

A. Simultaneous recording of reflection and transmission mode spectra and optical data for silver

Figure 7 shows a typical FECO pattern recorded for two equally thick mica layers in contact, coated with a 32 nm silver mirror (as fitted using the iterative process described above). These data are recorded in the newly designed optics shown in Fig. 2. It shows the first ever recorded transmission (a) and reflection (b) mode data for exactly the same contact of a standard 3 layer interferometer used in SFA. So far, only the reflection mode spectra of a bulk metallic liquid facing a back-silvered mica have been demonstrated.[17] Analysis of the thickness of the mica using either the reflection mode or the transmission mode signal results in deviations of less than 0.01% of the total mica thickness.

With an optimized optics, it is hence possible to work in either reflection or transmission mode without any compromise in resolution of the spectra. This opens up a number of new possibilities for setting up SFA experiments. It is now possible to record FECO and NR in the reflection mode, while leaving the room for the transmission path to perform simultaneous complementary analysis, including, for instance, fluorescence microscopy.

Figure 7(d) also shows that the implemented 4 × 4 matrix approach, together with a white light correction, can effectively model spectra with high accuracy. Interestingly, recorded reflection mode FECO show a distinctly non-Lorentz-like peak shape with considerable tailing toward longer wavelengths. This experimentally observed spectral feature strongly depends on the wavelength dependent refractive index of the silver layers and, in particular, on the imaginary part. We cannot simulate this spectral behavior well with wavelength independent refractive indices or with any other data sets for silver available in the databases and literature. This suggests that the data set that we use for silver is particularly well suited for modeling thin films of silver used in SFA experiments (optical data file included in the supplementary material).

B. Thickness of confined molecular layers, radius calibration, and force-distance characteristics

Figure 8 summarizes the performance of the new optics and the 4 × 4 matrix analysis for the essential standard SFA experiment. Here, we performed a force vs distance measurement and analysis of a supported lipid monolayer facing a mica surface. For this purpose, we supported the lipid layer with an inner hydrophobic self-assembled monolayer (SAM) on gold, followed by the LB-deposition of an outer layer of the neutral DPPC lipid, which together can be described as a bilayer-type structure, referred to as a bilayer for simplicity. This is a benchmark experiment in many respects, as it involves a number of critical steps in the analysis and experiment, which are summarized in the flow chart of an SFA experiment in Fig. S1(f) of the supplementary material.

First, an initial contact referencing for a clean mica gold contact is performed.

This is followed by removal of the gold disc from the SFA chamber for a >12 h thiol deposition. After successful thiol deposition, the gold, now coated with a self-assembled monolayer, is transferred back to the SFA chamber for measuring the thickness

Transmission FECO
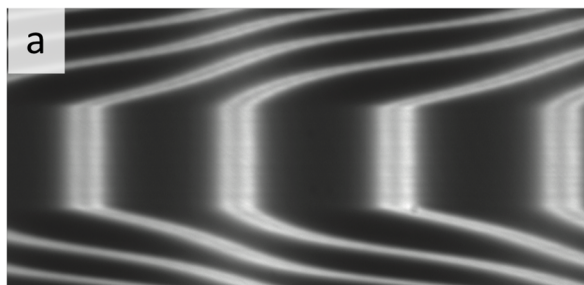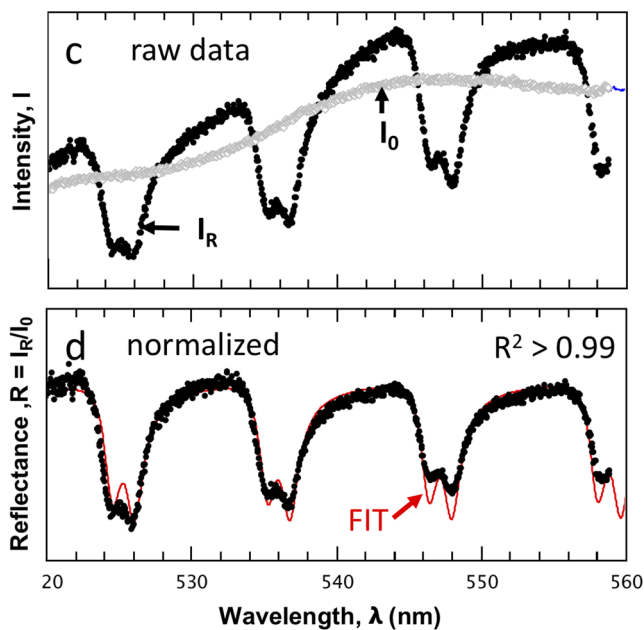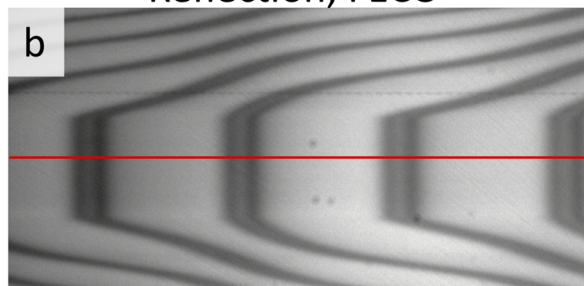

Reflection, FECO

FIG. 7. Comparison of (a) FECO recorded in the transmission mode and (b) reflection mode for the same contact between two mica sheets with a 32 nm silver mirror at their backsides. The data [(c), raw data] extracted from the line indicated in (b) show the recorded intensity of the white light, I_0, and the FECO, I_R. [(d), normalized] shows the calculated reflectance, $R = I_R/I_0$, and a fit (solid red line) with a fit quality of $R^2 > 0.99$.

of the SAM. Here, we find a consistent thickness of 1.2 ± 0.2 nm taking into account all aspects mentioned above. This agrees very well with reported thicknesses and tilt angles of this particular SAM and ellipsometry data of such thin films.[52–55]
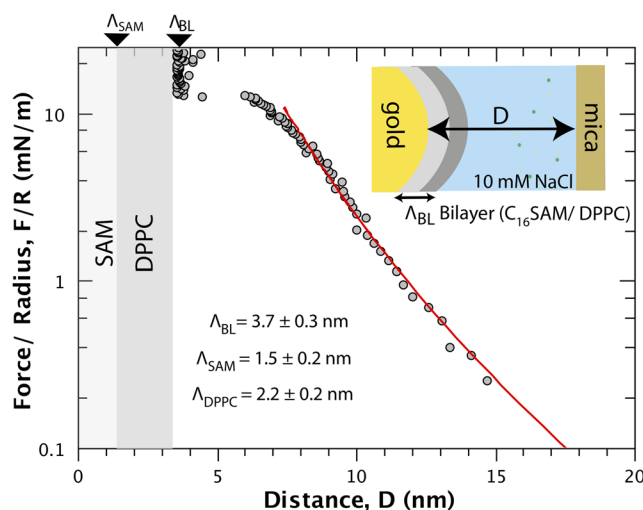

FIG. 8. Force vs distance characteristics of a lipid bilayer-type model facing a bare mica surface in 10 mM NaCl solution. The schematic details the optical layer (interferometer) setup in this experiment. A molecularly smooth gold surface is modified with a hydrophobic hexadecane-1-thiol SAM, followed by coating with an outer DPPC layer in the gel phase. The distance $D = 0$ is defined as contact between gold and mica in dry nitrogen. The SAM thickness T_{SAM} and bilayer thickness T_{BL} are indicated (cf. the text for details).

It should be noted that transfer out of the system is critical as a realignment of the contact with the optical path is necessary again. Using the newly designed optics (Fig. 2), we only move any newly established contact back to the optimized beam path and no errors can occur.

After establishing the SAM thickness, the SAM-covered gold is transferred to the LB-trough for the DPPC deposition. The deposited DPPC layer is transferred back to the SFA chamber under fully wet conditions, and the thickness of the constructed bilayer in solution and the force vs distance characteristics are measured. The force vs distance characteristics in Fig. 8 indicate a long range electric double layer repulsion that can be fitted well using a DLVO model. As expected, the data indicate a jump into a very adhesive contact, with a stable hard wall at the distance D that equals the thickness of the hydrated bilayer slab. Detailed outcomes of this particular interaction experiment and setup will be discussed elsewhere.

The measured and analyzed thickness of the SAM/DPPC layer is 3.2 ± 0.3 nm, indicating a hydrated DPPC thickness of 2 ± 0.2 nm, which agrees very well with previously observed and measured single layer thicknesses in a hydrated neutral bilayer.[28] An aspect worth mentioning is that we also optimized both refractive index and thickness of the established molecular layers using the iterative fitting approach described above and find that refractive indices of n = 1.478 for the molecular ordered thin films describe the observed spectra best.[39]

In a standard SFA setup, the interferometer is not sensitive to detect differences of in-plane/out of plane refractive indices of confined lipid like films. Simulations indicate peak shifts below the detection limit, if the refractive index is considered as anisotropic with refractive index differences of 0.04 for lipids. Hence, the data
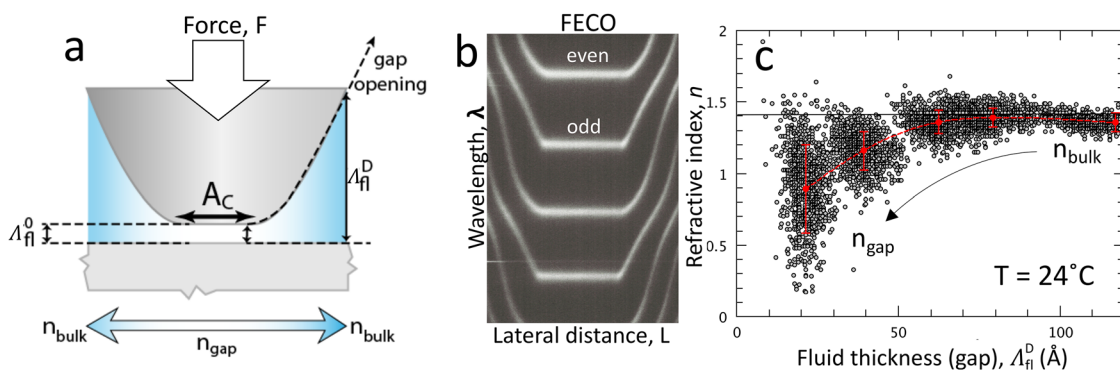
FIG. 9. (a) Schematic of a contact established in cyclohexane, indicating the contact area A_C, the fluid thickness Λ_{fl} in the gap, and in the gap opening where the surface-to-surface distance increases to Λ_{fl}^D. (b) shows the FECO pattern recorded and rotated to resemble the schematic in (a). (c) shows the simultaneous fit of the real part of the refractive index $\tilde{n}$ and the distance D as a function of the fluid thickness in the gap opening. The data were recorded at 24 °C, and the bulk cyclohexane refractive index is indicated. A clear decrease in n and increasing fluctuations at smaller gap sizes are observed.

are described equally well using an isotropic refractive index for the organic thin films. For materials such as liquid crystals, with refractive index differences of up to 0.2 for in-plane and out-of-plane, it is possible to distinguish anisotropy in confined thin films down to sub 10 nm gap thicknesses D.

C. Refractive index of fluids confined into a crevice

While the SFA is not sensitive to small changes of in-plane and out-of-plane refractive indices, it is very sensitive to isotropic refractive index changes of confined fluids down to molecular dimensions. Therefore, we fit refractive index changes of fluids confined into a crevice generated using the SFA.

This is a very interesting question in many fields, including crack propagation in stress corrosion cracking, where fluid properties at the crack tip are unknown, or for crevice corrosion, where fluid compositions within a crevice are often composed of salt solutions with concentrations close to saturation levels.

Figure 9(a) shows a cross section across an established contact between two mica sheets. Figure 9(b) shows a typical FECO pattern recorded and rotated by 90° to resemble the cross-sectional view.

After establishing a contact, we introduced cyclohexane and recorded >1000 FECO patterns with 10 frames/s. Figure 9(c) shows the result of simultaneously fitting both the real part of the refractive index and the fluid thickness (i.e., the gap thickness), using a look-up table approach, when going from the fully confined zone toward the gap opening as indicated in Fig. 9(a).

As previously described by Heuberger *et al.*,[56] we find a considerably lower refractive index at small fluid thicknesses, with an average (over 1000 frames, i.e., 100 s measurement time) that decreases to a value close to $n = 1$ at $\Lambda_{gap} = 2$ nm. This has previously been explained as a decreasing density, i.e., gas-like behavior, which is similarly confirmed by these data.

Interestingly, and also similar to observations by Heuberger *et al.*,[23] we find an increasingly broad refractive index distribution when going to small gap openings. This is consistent with the interpretation of considerable density fluctuations of the highly volatile cyclohexane when confined between two apposing hard walls.

However, at gap thicknesses below 2 nm, we find unexpected large variations resulting in refractive indices and standard deviations that extend well below 1.0. This may be due to a breakdown of continuum theory at such small gap thicknesses or due to reaching resolution limitations for relative peak shifts in the range of 0.02–0.04 nm spectral resolution in our systems. This effect will be studied in future work.

In summary, MBI provides a very detailed view of fluids confined into a gap or crack. The 4 × 4 matrix approach, together with a full fitting of FECO data, can provide refractive indices of nanometer confined fluids, with the possibility to include anisotropic layering that may arise in particular during confinement. Figure S7 of the supplementary material simulates expected spectral differences due to a change from an isotropic to anisotropic thin film, with typical anisotropic refractive indices for a liquid crystal and a lipid layer. We find that relative peak shifts of even and odd ordered fringes with respect to each other approach the conservative estimate of a spectral resolution of 0.04 nm at film thicknesses of 20 nm for lipids, and about 6 nm for liquid crystals. However, SFA may be sensitive to anisotropic refractive indices of monolayers of liquid crystals of 2 nm thickness and lipid layer thicknesses of 4 nm only if a resolution limit of 0.01 nm is achieved. This is possible with appropriate choices of optical components and will be subject to further studies.

VI. DISCUSSIONS AND CONCLUSIONS

A. Practical implications for SFA experiments

Based on the above data and analysis, a number of practical guidelines for performing SFA experiments can be extracted. These can be summarized as follows:

1. An optimized SFA experimental and data flow/analysis flow chart is shown in Fig. S1 of the supplementary material. The general procedure for obtaining best fitting results of experimental data is to first optimize azimuthal angle, birefringence, mirror thicknesses, as well as initial mica thickness from a contact measurement using an initial guess of the mica refractive index.

2. Azimuthal angles of apposing micas and birefringence can be directly interpreted from a visual inspection of the peak splitting which enables a close approximation to be input in the initial fitting parameters. Relative intensities of β- and γ-fringes indicate the relative rotation of the mica layers, and birefringence is a direct measure of the beta-gamma splitting.

3. The mica refractive index and the resulting mica thickness can be refined to accuracy in the 4th digit for the individual mica sheets, using a set of spectra with an added isotropic gap layer. Since mica is a natural material with considerable variations of the refractive index, it is recommended to fit the refractive index. Only this provides an absolute evaluation of layer thicknesses, specifically at larger separation distances. We find variations from 1.52 up to 1.61 depending on the batch of mica, with most micas being in a smaller range around 1.58 ± 0.02.

4. Upon change of contact positions, an accurate fitting of the metal mirror thickness can eliminate systematic errors due to small variations in the metal mirror thicknesses. In addition, using a fixed and aligned optical path, and a translation mechanism for moving established contacts into the beam path (described in Fig. 2) minimizes systematic errors due to small deviations of optical alignments after, e.g., the contact position changes.

5. It is useful and often essential (e.g., in reflection mode operation or with metal mirrors that can corrode) to simultaneously record a white light reference spectrum for providing normalized data analysis of full spectra. This can be easily achieved using an optical path described in Fig. 2.

6. Glue layers can be safely neglected in a simulation approach in the green and yellow wavelength region as long as a spectral resolution below 0.02 nm is not achieved.

B. Accuracy and potential for automation and real-time analysis

The typical fitting error of a full spectral fitting is in the range of 0.09%, for a mica thickness of 10 μm. The determination of a bilayer thickness from a single experiment results in a standard deviation of 50 pm. Fitting a full spectrum for an ideal layer thickness and isotropic refractive index within a small window typically requires that about 10–20 spectra are calculated and fitted. As a result, a full fitting approach is inherently slow, with possible frame rates in the range of seconds. This is clearly too slow for a typical video acquisition rate of 10–30 Hz for SFA spectra. Here, the fast correlation spectroscopy and analytical equations analyzing only the wavelength maxima provide a fast and straight forward solution, with the discussed caveats of not fitting intensities and peak shapes. However, this may be combined in a postexperimental analysis.

In order to speed up online analysis, we implemented a fast full spectral fitting approach based on a "look-up table" approach. Such an approach provides a simulation of all possible spectra within a given grid of refractive indices (Δn) and layer thicknesses ($\Delta\Lambda$). This takes about 20–30 min to compute on a standard desktop PC and much less on a supercomputer, using a window of interest for a typical SFA experiment with $\Delta n = \pm 0.50$ and $\Delta\Lambda = 0.00$–100.00 nm. The resulting 2–5 MB look-up table can be easily stored in memory for a fast direct comparison with measured spectra. Based on calculating

and comparing the sum of residual squares for spectra within a reasonable range of the previous spectrum, the best fit is chosen within a few millisecond, providing online capabilities much faster compared to typical 10–30 fps video frame rates of SFA data recording. Look-up tables can be saved, stored, and recalled into other real-time software, which offers the possibility to implement this into an SFA feedback regulation. This is beyond the scope of this article and will be discussed in a future study.

C. Conclusions

In summary, we implemented and tested new optics and the 4×4 transfer matrix approach by Schubert[26] for acquisition and simulation, respectively, of full transmission and reflection mode MBI patterns obtained in a variety of different SFA experiments. A numerical fitting approach for calculation of partial transfer matrices for anisotropic layers was developed and implemented, and an optimized experiment and analysis data flow were developed for SFA experiments in order to reduce systematic errors (see Fig. S1 of the supplementary material). We demonstrated the performance of the Schubert method using a number of benchmark experiments, including the full description of birefringent layers, the consecutive fitting of thicknesses of deposited chemical modification layers, and the measurement of refractive indices of cyclohexane confined within a nanometer gap. We further discussed the simulation of the rotation angle of two apposing birefringent mica layers, fitting of reflection mode spectra, and simulation and fitting of metal mirror thicknesses for the minimization of systematic experimental errors in SFA. The analysis procedure introduced here makes SFA an absolute technique, not only with respect to an optical reference thickness but with respect to the dimensions of the full stacks of materials in the interferometer cavity, and enables a more detailed insight into SFA data.

The newly developed optical layout for SFA, which simplifies operation, introduces reference beams, allows recording of reflection and transmission mode spectra, and minimizes potential systematic errors in experiments and analysis. This approach greatly simplifies SFA experimentation and analysis and opens SFA for new and exciting opportunities, including metamaterials, multilayered anisotropic layers, layers of rotating anisotropic layer, as well as chiral layers, for which partial transfer matrices are readily available from Schubert's original work.

SUPPLEMENTARY MATERIAL

See supplementary material for a brief review of analytical and transfer matrix based analysis methods used in SFA, a photograph of the experimental setup, simulations of an interferometer with asymmetric glue thicknesses, and comparison of spectral resolution limit for anisotropic layers, along with the optical material data file for silver used throughout this study.

ACKNOWLEDGMENTS

REFERENCES

[1] S. Tolansky, "Interferometric evaluation of thicknesses of thin films," J. Phys. Radium **11**(7), 373–374 (1950).

[2] D. Tabor and R. H. Winterton, "Surface forces: Direct measurement of normal and retarded van der Waals forces," Nature **219**(5159), 1120 (1968).

[3] D. Tabor and R. H. Winterton, "Direct measurement of normal and retarded van der Waals forces," Proc. R. Soc. A **312**(1511), 435 (1969).

[4] J. N. Israelachvili, "Thin film studies using multiple-beam interferometry," J. Colloid Interface Sci. **44**(2), 259–272 (1973).

[5] J. N. Israelachvili and D. Tabor, "Measurement of van der Waals dispersion forces in range 1.4 to 130 nm," Nat. Phys. Sci. **236**(68), 106 (1972).

[6] J. N. Israelachvili and R. M. Pashley, "The hydrophobic interaction is long-range, decaying exponentially with distance," Nature **300**(5890), 341–342 (1982).

[7] J. N. Isrealachvili and R. M. Pashley, "Molecular layering of water at surfaces and origin of repulsive hydration forces," Nature **306**(5940), 249–250 (1983).

[8] J. N. Israelachvili, R. K. Tandon, and L. R. White, "Measurement of forces between 2 mica surfaces in aqueous poly(ethylene oxide) solutions," Nature **277**(5692), 120–121 (1979).

[9] L. R. Fisher and J. N. Israelachvili, "Direct experimental-verification of the Kelvin equation for capillary condensation," Nature **277**(5697), 548–549 (1979).

[10] J. N. Israelachvili and G. E. Adams, "Measurement of forces between 2 mica surfaces in aqueous electrolyte solutions in range 0-100 nm," J. Chem. Soc., Faraday Trans. 1 **74**(4), 975 (1978).

[11] J. N. Israelachvili, Y. Min, M. Akbulut, A. Alig, G. Carver, W. Greene, K. Kristiansen, E. Meyer, N. Pesika, K. Rosenberg, and H. Zeng, "Recent advances in the surface forces apparatus (SFA) technique," Rep. Prog. Phys. **73**(3), 036601 (2010).

[12] S. H. Donaldson, Jr., M. Valtiner, M. A. Gebbie, J. Haradad, and J. N. Israelachvili, "Interactions and visualization of bio-mimetic membrane detachment at smooth and nano-rough gold electrode surfaces," Soft Matter **9**(21), 5231–5238 (2013).

[13] C. Pick, C. Argento, G. Drazer, and J. Frechette, "Micropatterned charge heterogeneities via vapor deposition of aminosilanes," Langmuir **31**(39), 10725–10733 (2015).

[14] M. Valtiner, S. H. Donaldson, Jr., M. A. Gebbie, and J. N. Israelachvili, "Hydrophobic forces, electrostatic steering, and acid-base bridging between atomically smooth self-assembled monolayers and end-functionalized pegolated lipid bilayers," J. Am. Chem. Soc. **134**(3), 1746–1753 (2012).

[15] M. Valtiner, X. Banquy, K. Kristiansen, G. W. Greene, and J. N. Israelachvili, "The electrochemical surface forces apparatus: The effect of surface roughness, electrostatic surface potentials, and anodic oxide growth on interaction forces, and friction between dissimilar surfaces in aqueous solutions," Langmuir **28**(36), 13080–13093 (2012).

[16] B. R. Shrestha, T. Baimpos, S. Raman, and M. Valtiner, "Angstrom-resolved real-time dissection of electrochemically active noble metal interfaces," ACS Nano **8**(6), 5979–5987 (2014).

[17] J. N. Connor and R. G. Horn, "Extending the surface force apparatus capabilities by using white light interferometry in reflection," Rev. Sci. Instrum. **74**(11), 4601–4606 (2003).

[18] C. Merola, H.-W. Cheng, K. Schwenzfeier, K. Kristiansen, Y.-J. Chen, H. A. Dobbs, J. N. Israelachvili, and M. Valtiner, "In situ nano- to microscopic imaging and growth mechanism of electrochemical dissolution (e.g., corrosion) of a confined metal surface," Proc. Natl. Acad. Sci. U. S. A. **114**(36), 9541–9546 (2017).

[19] B. R. Shrestha, Q. Hu, T. Baimpos, K. Kristiansen, J. N. Israelachvili, and M. Valtiner, "Real-time monitoring of aluminum crevice corrosion and its inhibition by vanadates with multiple beam interferometry in a surface forces apparatus," J. Electrochem. Soc. **162**(7), C327–C332 (2015).

[20] J. M. Levins and T. K. Vanderlick, "Extended spectral-analysis of multiple-beam interferometry," Langmuir **10**(7), 2389–2394 (1994).

[21] M. T. Clarkson, "Multiple-beam interferometry with thin metal films and unsymmetrical systems," J. Phys. D: Appl. Phys. **22**(4), 475–482 (1989).

[22] M. Born and E. Wolf, Principles of Optics, 4th ed. (Pergamon Press, 1970), Chap. 1.6.2.

[23] M. Heuberger, "The extended surface forces apparatus. Part I. Fast spectral correlation interferometry," Rev. Sci. Instrum. **72**(3), 1700–1707 (2001).

[24] M. Zach, J. Vanicek, and M. Heuberger, "The extended surface forces apparatus. Part III. High-speed interferometric distance measurement," Rev. Sci. Instrum. **74**(1), 260–266 (2003).

[25] B. Zappone, W. Zheng, and S. Perkin, "Multiple-beam optical interferometry of anisotropic soft materials nanoconfined with the surface force apparatus," Rev. Sci. Instrum. **89**(8), 085112 (2018).

[26] M. Schubert, "Polarization-dependent optical parameters of arbitrarily anisotropic homogeneous layered systems," Phys. Rev. B **53**(8), 4265–4274 (1996).

[27] D. F. Kienle and T. L. Kuhl, "Analyzing refractive index profiles of confined fluids by interferometry," Anal. Chem. **86**(23), 11860–11867 (2014).

[28] D. F. Kienle and T. L. Kuhl, "Analyzing refractive index profiles of confined fluids by interferometry part II: Multilayer and asymmetric systems," Anal. Chim. Acta **936**, 236–244 (2016).

[29] M. Newville, A. Nelson, A. Ingargiola, T. Stensitzki, D. Allan, Michał, Glenn, Y. Ram, M. Smiles, L. Li et al. (2016). LMFIT: Non-Linear Least-Square Minimization and Curve-Fitting for Python (Zenodo, 2016).

[30] Winpython Development Team, WinPython, 2017.

[31] A. Lizardo, B. Araujo, H. Parente Lima, L. Moura, L. M. Wolf, M. Lira, P. Alcantara, R. A. O. Filho, and W. Moreira, PySide, 2016.

[32] T. E. Oliphant, Guide to NumPy, 2nd ed. (CreateSpace Independent Publishing Platform, Provo, UT, 2015), ISBN: 978-1-5173-0007-4.

[33] E. Jones, T. Oliphant, P. Peterson et al., SciPy: Open source scientific tools for Python, 2001.

[34] wiredfool, A. Clark, Hugo, A. Murray, A. Karpinsky, C. Gohlke, B. Crowell, D. Schmidt, A. Houghton, S. Johnson, S. Mani, J. Ware, D. Caro, S. Kossouho, E. W. Brown, A. Lee, M. Korobov, M. Górny, E. Santana Santana, N. Pieuchot, O. Tonnhofer, M. Brown, B. Pierre, J. Cuenca Abela, L. J. Solberg, F. Reyes, A. Buzanov, Y. Yu, eliempje, and F. Tolf, Pillow: 4.0.0, January 2017.

[35] L. Campagnola, PyQtGraph, 2017.

[36] A. D. Rakić, A. B. Djurišic, J. M. Elazar, and M. L. Majewski, "Optical properties of metallic films for vertical-cavity optoelectronic devices," Appl. Opt. **37**, 5271–5283 (1998).

[37] I. Z. Kozma, P. Krok, and E. Riedle, "Direct measurement of the group-velocity mismatch and derivation of the refractive-index dispersion for a variety of solvents in the ultraviolet," J. Opt. Soc. Am. B **22**, 1479–1485 (2005).

[38] G. M. Hale and M. R. Querry, "Optical constants of water in the 200-nm to 200-μm wavelength region," Appl. Opt. **12**, 555–563 (1973).

[39] D. F. Kienle, J. V. de Souza, E. B. Watkins, and T. L. Kuhl, "Thickness and refractive index of DPPC and DPPE monolayers by multiple-beam interferometry," Anal. Bioanal. Chem. **406**(19), 4725–4733 (2014).

[40] I. H. Malitson, "Interspecimen comparison of the refractive index of fused silica," J. Opt. Soc. Am. **55**(10), 1205–1209 (1965).

[41] P. E. Ciddor, "Refractive index of air: New equations for the visible and near infrared," Appl. Opt. **35**, 1566–1573 (1996).

[42] M. Polyanskiy, https://refractiveindex.info, 2018.

[43] Norland Products, Product data sheet for NOA81, 2019.

[44] A. I. Bailey and S. M. Kay, "Measurement of refractive index and dispersion of mica, employing multiple beam interference techniques," Br. J. Appl. Phys. **16**, 39–44 (1965).

[45] D. W. Lee, K. Kristiansen, S. H. Donaldson, Jr., N. Cadirov, X. Banquy, and J. N. Israelachvili, "Real-time intermembrane force measurements and imaging of lipid domain morphology during hemifusion," Nat. Commun. **6**, 7238 (2015).

[46] S. de Beer, D. 't Mannetje, S. Zantema, and F. Mugele, "Instability of confined water films between elastic surfaces," Langmuir **26**(5), 3280–3285 (2010).

[47] F. Mugele and M. Salmeron, "Dynamics of layering transitions in confined liquids," Phys. Rev. Lett. **84**(25), 5796–5799 (2000).

[48] F. Mugele, S. Baldelli, G. A. Somorjai, and M. Salmeron, "Structure of confined films of chain alcohols," J. Phys. Chem. B **104**(14), 3140–3144 (2000).

[49] C. D. van Engers, M. Balabajew, A. Southam, and S. Perkin, "A 3-mirror surface force balance for the investigation of fluids confined to nanoscale films between two ultra-smooth polarizable electrodes," Rev. Sci. Instrum. **89**(12), 123901 (2018).

[50] W. M. Moore and P. J. Codella, "Oxidation of silver films by atomic oxygen," J. Phys. Chem. **92**(15), 4421–4426 (1988).

[51] L.-K. Chau and M. D. Porter, "Composition and structure of spontaneously adsorbed monolayers of n-perfluorocarboxylic acids on silver," Chem. Phys. Lett. **167**(3), 198–204 (1990).

[52] K. B. Rodenhausen, B. A. Duensing, T. Kasputis, A. K. Pannier, T. Hofmann, M. Schubert, T. E. Tiwald, M. Solinsky, and M. Wagner, "*In situ* monitoring of alkanethiol self-assembled monolayer chemisorption with combined spectroscopic ellipsometry and quartz crystal microbalance techniques," in *5th International Conference on Spectroscopic Ellipsometry (ICSE-V)* [Thin Solid Films **519**(9), 2817–2820 (2011)].

[53] D. Peev, T. Hofmann, N. Kananizadeh, S. Beeram, E. Rodriguez, S. Wimer, K. B. Rodenhausen, C. M. Herzinger, T. Kasputis, E. Pfaunmiller, A. Nguyen,

R. Korlacki, A. Pannier, Y. Li, E. Schubert, D. Hage, and M. Schubert, "Anisotropic contrast optical microscope," Rev. Sci. Instrum. **87**(11), 113701 (2016).

[54] K. B. Rodenhausen, T. Kasputis, A. K. Pannier, J. Y. Gerasimov, R. Y. Lai, M. Solinsky, T. E. Tiwald, H. Wang, A. Sarkar, T. Hofmann, N. Ianno, and M. Schubert, "Combined optical and acoustical method for determination of thickness and porosity of transparent organic layers below the ultra-thin film limit," Rev. Sci. Instrum. **82**(10), 103111 (2011).

[55] K. B. Rodenhausen and M. Schubert, "Virtual separation approach to study porous ultra-thin films by combined spectroscopic ellipsometry and quartz crystal microbalance methods," in *5th International Conference on Spectroscopic Ellipsometry (ICSE-V)* [Thin Solid Films **519**(9), 2772–2776 (2011)].

[56] M. Heuberger, M. Zach, and N. D. Spencer, "Density fluctuations under confinement: When is a fluid not a fluid?," Science **292**(5518), 905–908 (2001).